ACCSCIENCE PUBLISHING

International Journal of Bioprinting

ACCEPTED PAPER · MAIN TEXT

Predictive machine learning models for printability assessment in extrusion-based 3D bioprinting

Article ID: IJB026320336

Citation: Isichei JC, Li S, Copus J, Lee SJ, Heyward I, Desai S. Predictive machine learning models for printability assessment in extrusion-based 3D bioprinting. *Int J Bioprint*. 2026. doi: 10.36922/IJB026320336

AccScience Publishing
RESEARCH ARTICLE
Volume X Issue X (2026)
doi: 10.36922/IJB026320336

Predictive machine learning models for printability assessment in extrusion-based 3D bioprinting

Running title: Machine learning for 3D bioprinting printability

Joan. C. Isichei[1], Siyuan Li[2], Joshua Copus[2], Sang Jin Lee[2], Izabele Heyward[1], and Salil Desai[1,2]*

[1] Industrial and Systems Engineering, North Carolina A&T State University, Greensboro, NC 27411, United States of America
[2] Wake Forest Institute for Regenerative Medicine, Wake Forest University School of Medicine, Medical Center Boulevard, Winston-Salem, NC 27157, United States of America

***Corresponding author:**
Salil Desai (sdesai@ncat.edu)

Citation: Isichei JC, Li S, Copus J, Lee SJ, Heyward I, Desai S. Predictive machine learning models for printability assessment in extrusion-based 3D bioprinting. *Int J Bioprint*. 2026. doi: 10.36922/IJB026320336

Received: August 4, 2026
Revised: September 4, 2026
Accepted: September 9, 2026
Published online: September 9, 2026

Abstract

Bioprinting has great potential in tissue engineering and regenerative medicine applications due to the possibility of creating functional tissue replacements for damaged tissues or organs. However, current methods for optimizing printing parameters are time-consuming and heavily rely on operators' experience. In this study, Pluronic F127 and sodium alginate-Laponite (Alg-Lap) bioinks were used to evaluate the quality of four bioprinted constructs: tubular, angular, crosshatch, and overhang structures. Machine learning (ML) algorithms, including Multilayer Perceptron (MLP), Random Forest (RF), Gaussian Naive Bayes (GNB), Classification and Regression Trees (CART), Support Vector Machines (SVM), and Logistic Regression (LR), were evaluated for classifying constructs into print-quality categories using pre-print parameters and post-print geometry-specific quality measurements. RF performed best for the tubular, crosshatch, and overhang structures, achieving classification accuracies of 91.9%, 95.3%, and 96.0%, respectively, while MLP performed best for the angular structure, achieving 96.3% accuracy. Balanced accuracies for these best-performing models were 85.8%, 91.8%, 86.9%, and 90.8% for the tubular, crosshatch, overhang, and angular structures, respectively. These findings demonstrate the potential of ML-based quality classification to support more reproducible assessment of extrusion-based bioprinting outcomes, advancing tissue engineering and regenerative medicine applications while enhancing efficiency and reproducibility.

Keywords: 3D bioprinting; Bioinks; Machine learning; Predictive models; Printability

1. Introduction

Bioprinting is a rapidly developing field that uses 3D printing technology to produce living tissue models with controlled architecture and function [1-3]. It has great potential to advance regenerative medicine by enabling the development of functional tissue replacements for damaged or diseased tissues and organs [4]. Considerable progress has been made in developing increasingly sophisticated tissue constructs using a variety of bioprinting strategies [5-9]. Despite these advances, bioinks that simultaneously satisfy biological and manufacturing requirements remain limited. An effective bioink, a hydrogel containing cells and signaling molecules, maintains high cell viability while supporting tissue development with adequate rheological and mechanical properties, enabling accurate and reproducible printing [10-14]. Therefore, bioink development focuses on achieving favorable biological performance and maintaining good printability.

Printability assessment has traditionally relied on qualitative or basic quantitative metrics, such as filament width. However, these methodologies often prove inadequate for analyzing intricate structures with sharp turns, curves, pores, and multilayer stacking [5, 15]. Critical parameters such as feed rate (or printing speed) and flow rate strongly influence material deposition during printing. Nevertheless, current approaches to optimizing printing parameters are time-consuming and heavily reliant on experiential knowledge [16–19]. Furthermore, all hydrogel-based bioink systems exhibit diverse, dynamic rheological behaviors and are susceptible to environmental factors such as temperature and humidity [20-21]. Although 3D printing processes are expected to be automated, these limitations make them labor-intensive. To address these challenges, leveraging machine learning (ML) holds promise.

The primary advantage of using ML in bioprinting, compared to traditional computational techniques, is its ability to predict the printing process precisely. This improves accuracy and reproducibility. By employing ML algorithms [22], artificial intelligence (AI) can optimize various printing parameters such as feed rate and flow rate [23-24]. Consequently, this optimization improves printing outcomes by anticipating the ideal printing conditions and design parameters for specific tissues or organs. Another significant benefit of integrating ML into bioprinting is reducing waste and minimizing errors. This efficiency is particularly apparent when ML automates the bioprinting process. Such automation significantly reduces the time and resources needed to produce desired

tissues or organs. Furthermore, ML/AI improves the cost-effectiveness of bioprinting by optimizing processes, minimizing material waste, and increasing overall efficiency [25].

Recent advances in bioprinting further emphasize the need for intelligent and adaptive approaches to control increasingly complex fabrication processes. Advanced strategies, including multimaterial, multimodal, in situ, and structure-guided bioprinting, enable the fabrication of constructs with improved anatomical relevance, biomimetic microenvironments, and cellular organization, while also increasing the complexity of material and process optimization [26]. For example, Huang et al. developed a nanoengineered extrusion-aligned tract (NEAT) bioprinting strategy that exploited printing-induced shear stress to generate highly aligned collagen-based constructs, showing how precisely controlled processing conditions can directly influence structural organization, cellular alignment, differentiation, and ultimately tissue function [27]. Recent developments in ML/AI provide complementary approaches for navigating such complex process–material relationships. Lee et al. highlighted the expanding use of AI/ML across bioink formulation, printability assessment, process monitoring, and post-print maturation, while also emphasizing the need for rigorous validation to ensure the reliability and generalizability of predictive models [28]. Moving beyond conventional classification and regression approaches, Zhang et al. developed an explainable generative AI framework coupled with Bayesian optimization to predict deposition morphology and identify printing defects within an in silico closed-loop optimization system [29]. Collectively, these advances show a shift toward data-driven and increasingly autonomous bioprinting, where predictive models can connect material properties and printing parameters to construct quality and biological performance.

Researchers have leveraged ML algorithms to refine bioprinting parameters such as speed, temperature, and deposition rate [30-38], thereby enhancing the precision and quality of 3D bioprinted structures. A recent investigation by Ruberu *et al.* explored the potential of ML to boost the printability of GelMA and GelMA/HAMA bioinks, achieving precise and consistent 3D outputs [39]. They applied Bayesian optimization to pinpoint optimal printing settings, significantly reducing the number of experimental iterations required to identify superior parameters. This method evaluated various bioink densities and printer configurations. A "black-box" model generated recommendations from visual evaluations of filament shapes and pore structures. This

innovative approach refined the conventional trial-and-error methodology, resulting in an optimal overall score.

Bonatti, Chua, and De Maria introduced an AI-driven quality control loop that dynamically adjusts printing settings based on the material and setup, and provides immediate feedback for adjustments [40]. This system aims to continuously optimize bioprinting parameters to adapt to various material types and configurations while monitoring adjustments in real time. Their research involved collecting extensive datasets, including video and critical bioprinting parameters such as layer height and infill density. They primarily used Pluronic F-127 bioink, adding color to simulate different materials. Another study by Conev *et al.* [41] implemented an ML algorithm to forecast printing quality across various settings. They compared two ML strategies using the Random Forest algorithm: one for classification and the other for regression. For baseline comparison, they also employed a straightforward linear regression model to gauge material precision. Their findings highlighted that multiple factors, including printing speed, material composition, and printing pressure, influence print quality.

Another successful application of ML in bioprinting is predicting cell and tissue behavior. ML algorithms have been used to analyze complex biological data and predict cell and tissue behavior. This prediction is crucial to creating functional tissues and organs. Rafieyan *et al.* [42] used ML to predict cell behavior on scaffolds for cardiac tissue engineering (CTE) applications by modeling an extensive dataset compiled from the existing literature, encompassing a variety of materials, cell lines, and fabrication methods, and considering viability, growth, proliferation, and differentiation when rating the scaffolds. After applying 28 ML algorithms, XGBoost performed well, achieving 87% accuracy. Ensemble learning with the five best-performing algorithms yielded 93% accuracy for the AdaBoost Classifier and Voting Classifier. In addition, the authors developed an open-source software tool, MLATE (Machine Learning Applications in Tissue Engineering), to help the broader scientific community use their models.

ML in bioprinting remains a significant challenge because of the complex interactions among biological, chemical, and physical variables, particularly when considering bioink printability [43]. Bioprinting aims to create functional tissue constructs by precisely depositing cells, biomaterials, and growth factors, a process that requires a deep understanding of how they interact. Despite these challenges, developing predictive models to assess bioink printability can enhance the bioprinting

process by identifying optimal parameters, reducing the need for extensive trial-and-error experiments [8, 20, 44], and identifying potential problems early. This predictive capability improves efficiency and precision, ensuring consistent, reliable tissue constructs and ultimately advancing regenerative medicine and personalized healthcare by increasing the sustainability and scalability of bioprinting.

Prior ML studies have demonstrated parameter optimization or quality prediction for individual bioinks, filament/pore metrics, or specific printing conditions. The present study aims to determine whether a set of pre-print extrusion parameters can classify print quality across multiple complex geometries. We selected four benchmark structures to probe different failure modes, including multilayer stacking and curvature, pore formation, sharp-turn fidelity, and unsupported spanning. By comparing six different classifiers that incorporate linear, probabilistic, kernel, tree-based, ensemble, and neural-network approaches and using two bioinks, this study proposes to evaluate the geometry dependence of predictive model performance and establish structure-specific models for printability screening. This framework enables the identification of whether different printing geometries require distinct predictive models despite being generated from the same set of pre-print extrusion parameters

Pluronic F127 and sodium alginate-laponite (Alg-Lap) bioinks were used to evaluate the quality of different bioprinted constructs: tubular, angular, crosshatch, and overhang structures. We selected these bioinks because they are widely used in bioprinting. Pluronic F127 and sodium alginate–laponite constitute complementary hydrogel systems for extrusion bioprinting because they meet multiple requirements for cytocompatibility, shear-mediated cell protection, filament stability, and construct maturation. Pluronic F127 has favorable properties for 3D printing because of its thermoresponsive behavior, stable viscosity at room and body temperatures, and common use as a sacrificial material in tissue engineering [45]. Pluronic bioinks show strong shear-thinning behavior, facile liquefaction to support perfusable channels, enhancing oxygen and nutrient transport [46] while maintaining high post-printing cellular viability. Sodium alginate provides a hydrated cytocompatible matrix supporting cell encapsulation. Adding laponite introduces reversible electrostatic polymer-particle interactions, enabling thixotropic recovery and minimizing mechanical injury to cells during extrusion bioprinting. An Alg-Lap composite hydrogel has excellent printability and mechanical stability, combining the biocompatibility

properties of sodium alginate with the enhanced viscosity, yield stress, and shear-thinning behavior of laponite [47]. Alg-Lap formulations have demonstrated higher cellular viability, metabolic activity, spheroid formation, and embedded nutrient proliferation [48]. Thus, a multimaterial strategy in which Pluronic F127 establishes removable vascular or architectural features [49] and alginate–Laponite forms the persistent cell-laden phase [50] can simultaneously enhance bioprinting fidelity and mass transport, creating conditions favorable for sustained cell viability and proliferation.

ML algorithms, including Multilayer Perceptron (MLP), Random Forest (RF), Gaussian Naive Bayes (GNB), Classification and Regression Trees (CART), Support Vector Machines (SVM), and Logistic Regression (LR), were used to predict the 3D objects' shape fidelity and quality based on process parameter inputs of material, feed rate, flow rate, and speed ratio. By integrating ML into the 3D printing process, this research aims to significantly reduce material wastage, optimize printing strategies, and enhance the overall efficiency and reliability of 3D printing technology. This study's findings are expected to provide valuable insights and practical guidelines for applying ML to improve quality control in bioprinting, leading to smarter, more efficient biomanufacturing practices.

2. Materials and methods

Figure 1 outlines the workflow of using ML to improve bioprinting outcomes. By systematically incorporating key process parameters and bioink properties into ML algorithms, this method aims to predict and refine bioprinting conditions, ensuring high precision and reproducibility in creating tissue constructs. The process in **Figure 1** begins with defining key process parameters such as material, feed rate, flow rate, and speed ratio, which influence the bioprinting of bioinks like Pluronic and Alg-Lap. These parameters are fed into the bioprinting process, and the resulting data undergoes preprocessing. The preprocessed data is then used to select and train ML algorithms. These algorithms predict bioprinting outcomes, which are then compared to assess model performance. The best-performing model is selected to provide bioprinting guidance, ensuring optimized and efficient bioprinting conditions.

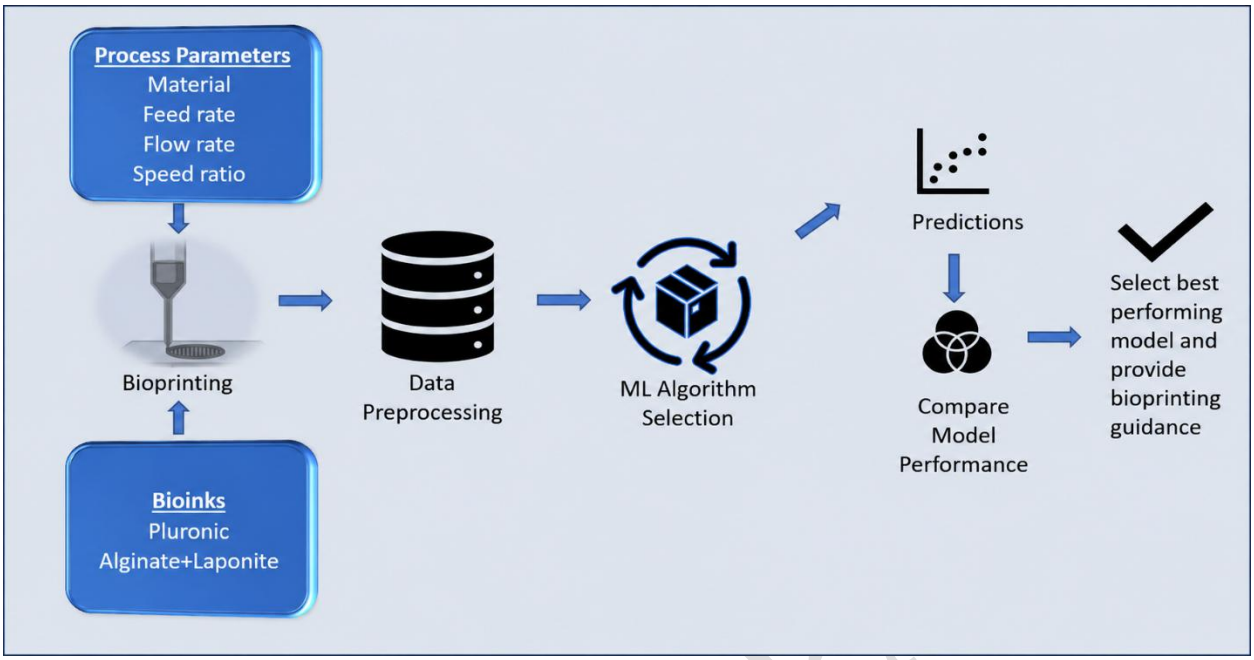

Figure 1. Bioprinting Predictive Modeling Process Flowchart.

2.1. Bioink preparation

All chemicals were purchased from Millipore Sigma (MO, USA) unless otherwise noted. In this study, two bioink formulations were used: (i) 40 wt% Pluronic F127 and (ii) 1 wt% sodium alginate mixed with 6 wt% Laponite RD (BYK USA Inc, TX, USA), which have been widely used and selected for standardized extrusion printing results [51]. To improve visualization, we aliquoted fluorescein dye and combined it with the bioinks to a final concentration of 0.01 mg of dye per milliliter of bioink. The formulation was transferred to the printing syringe, set in ice water for 5 min, and then equilibrated at 19 °C for 10 min.

2.2. Printability assessment

We evaluated printability using a specialized Integrated Tissue-Organ Printer (ITOP) system (see **Figure 2**). This system includes an XYZ stage/controller, a sterilized, sealed chamber, and a dispensing module. The motion controller and the XYZ three-axis stage system managed the nozzle printing trajectories. The dispensing apparatus included a precision pneumatic pressure controller, a temperature-regulated sleeve, a syringe, and a 510 μm cylindrical nozzle (Musashi Engineering, Inc., Tokyo, Japan). An acrylic enclosure formed the sealed chamber and included an environmental temperature control unit (EIC Solutions, Inc., Warminster, PA). A custom text-

based motion program accepted input for feed rate, pressure, nozzle trajectory, and additional printing parameters. This program was then uploaded to the printer's operating system to initiate printing. Flow rate determination involved a sequence of steps: a 30-second bioink extrusion, timing the extrusion, weighing the extruded substance, calculating weight per extrusion time, and then converting this weight to volume using a density of 1 mg/mm^3. We adjusted pressure to achieve the desired flow rate. Another evaluated parameter was the speed ratio, which equals the flow rate divided by the feed rate and represents the theoretical cross-sectional area of the printed material [52]. (**Table 1**) presents the obtained values of flow rate, feed rate, and the calculated speed ratio.

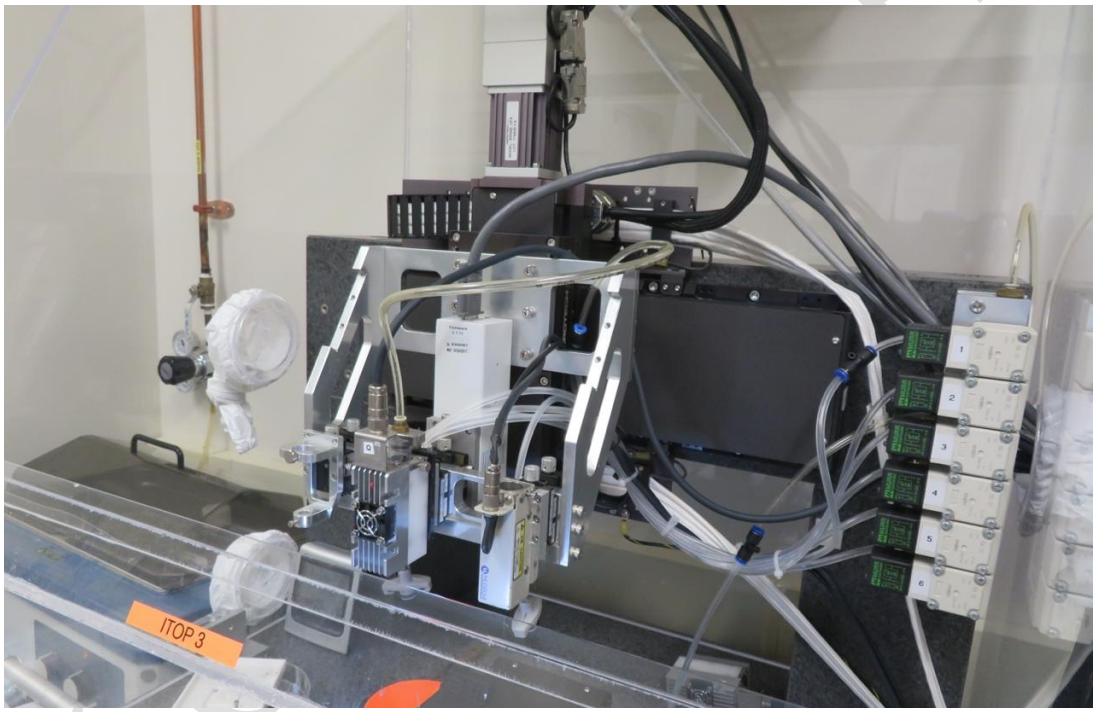

Figure 2. Integrated Tissue-Organ Printer (ITOP) system.

Table 1. Testing printing conditions range: feed rates, flow rates, and speed ratios.

Speed ratio $(\mathbf{mm^2}) = \frac{\boldsymbol{Flow\ rate}}{\boldsymbol{Feed\ rate}}$		**Flow rate (mm^3/min)**				
		21	**42**	**84**	**168**	**336**
Feed rate (mm/min)	**37.5**	0.56	1.12	2.24	4.48	8.96
	75	0.28	0.56	1.12	2.24	4.48
	150	0.14	0.28	0.56	1.12	2.24

	300	0.07	0.14	0.28	0.56	1.12
	600	0.035	0.07	0.14	0.28	0.56

This study considered four designs: tubular, crosshatch, overhang, and angular. **Table 2** presents the printing geometries and quantitative evaluation criteria used to assess printability for each structure. A prior study [53] presented details of the printability evaluations.

Table 2. Printing geometries and quantitative evaluation criteria used to assess printability for each structure.

Structure	Printing code	Evaluation criteria
Tubular	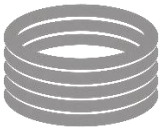 5-layer tube (top and side view)	• Height • Maximum width
Crosshatch	 Interlocking-line pattern (top view)	• Circularity (Pr) • Pore area
Overhang	 Overhang collapse (top view)	• Angle of deflection • Spanning success
Angular	 4-angled pattern (top view)	• Angle of corners • Filament width • Standard deviation of filament width • Left, right, and straight length of filament segment

The tubular structure consisted of a five-layer cylindrical structure with a 4 mm radius and was used to assess multilayer stacking and curved printing trajectories. From side-view images of the printed structures, we measured the structure's height and width. We averaged the height measurement over the central 75% of the structure to minimize edge variations, while recording the width at its maximum near the structure's base. The total layer heights for this five-layer

structure varied according to the speed ratios used (0.07, 0.14, 0.28, 0.56, 1.12, and 2.24 mm^2), resulting in layer heights of 0.15, 0.21, 0.32, 0.42, 0.53, and 0.75 mm, respectively

The crosshatch design featured a 2.67 mm line-pitch zigzag pattern rotated 90 degrees to create 9 square pores. From a top view, we quantified the area and circularity (Pr) value for each pore. We counted broken and filled pores. Pores completely filled were classified as "filled," while those with broken filaments on any side were marked as "broken." Pr was calculated as follows for all full, unfilled pores:

$$Pr = \frac{L^2}{16A} \qquad \text{(I)}$$

where L is the length, and *A* is the area.

The overhang structure was designed to evaluate the length of bioink that can span without support and the deflection angle at the midpoint. The gaps between supporting pillars are 16 mm, 8 mm, 4 mm, 2 mm, and 1 mm, respectively. The supporting pillars are 4 mm high. The angle of deflection was measured from the lowest deflection point to one supporting pillar of that gap, as the vertex of the angle, and ended at the other pillar.

$$\theta_d = sin^{-1}\left(\frac{D}{0.5G}\right) \qquad \text{(II)}$$

Where θ_d is the angle of deflection, D is the deflection at midpoint, and G is the gap length.

The angular structure, a four-angle pattern, was designed to evaluate the filament width and the accuracy of printing sharp turns. From the top view, we directly measured filament width on the left, right, and straight sections of each print. From these three measurements, we calculated the standard deviation of filament width. We determined the corner angle by counting the number of detectable angles in the structure.

$$\sigma_w = \sqrt{\frac{\sum(w_i-\mu)^2}{N_w}} \qquad \text{(III)}$$

Where σ_w is the standard deviation of the measured filament width, w_i is each filament width measurement, μ is the mean, and N_w is the total number of filament width measurements.

2.3. Dataset description

We constructed a separate dataset for each of the four 3D bioprinted constructs: tubular, crosshatch, overhang, and angular structures. Each record represented one independently printed part and contained the printing conditions, geometry-specific measurements obtained from the printed part, and the assigned print-quality class. **Table 3** presents the print-quality class by structure. **Figure 3** depicts images of all structures corresponding to each print quality definition: "Best", "Okay", and "Bad". The total number of data points used to run the ML models to predict bioprinted construct quality outcomes with Pluronic and Alg-Lap bioinks varied significantly across bioprinted structures. The final development datasets contained 1240 tubular, 1165 crosshatch, 1212 angular, and 1210 overhang samples, split into 70% training, 10% validation, and 20% testing. This variation was primarily because some experiments did not yield viable print outcomes, reducing the dataset for those structures.

Table 3. Tubular, crosshatch, overhang, and angular structure print quality level definition.

	Definition		
	Best	**Okay**	**Bad**
Tubular	Tube Height >= 2.16mm and Tube width between 9.09mm and 9.67mm.	Tube Height >= 2.16mm and Tube Width < 9.09mm or > 9.67mm	Tube Height < 2.16mm and Tube Width < 9.09 or > 9.67mm.
Crosshatch	Broken Pores = 0 Filled Pores = 0. 0.9 < Pr Value < 1.6 Area of Pore ≤ 3.3mm^2 (Pluronic) Area of Pore ≤ 2.9 mm^2(Alg-Lap)	Broken Pores = 0 Filled Pores = 0 0.9 < Pr Value <1.6 Area of Pore > 3.3mm^2 (Pluronic) Area of Pore > 2.9 mm^2 (Alg-Lap)	Broken Pores > 0 Filled Pores > 0 Pr Value = 0
Overhang	Pass1-Pass5 = 1 0 < Deflection1 < 1.6mm	Pass1-Pass5 = 1 Deflection1 ≥ 1.6mm	All or either of 5 Pass values =0 All or either of 5 Deflection values = 0
Angular	Turn1-Turn4 = 1 Thickness > 0.95mm	Turn1-Turn4 = 1 0 < Thickness < 0.95mm	All or either of 4 Turn Values = 0 Thickness = 0

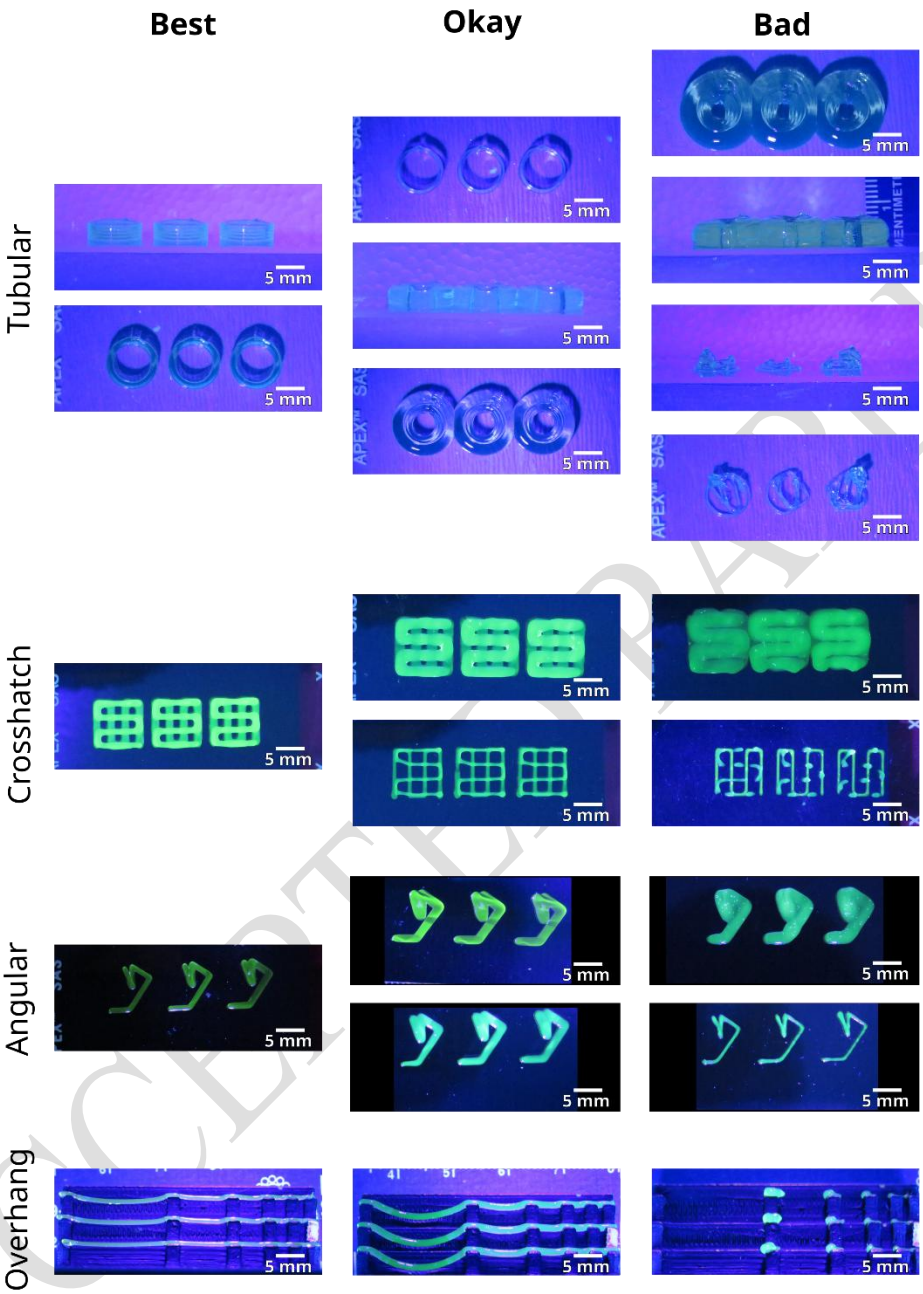

Figure 3. Examples of printed geometries used for printability assessment and ML classification for tubular, crosshatch, angular, and overhang structures. Each bioprinted construct was classified as “Best”, “Okay”, or “Bad” based on the print quality level definition.

2.4. Model building

MLP, SVM, CART, GNB, RF, and LR models were selected because they have demonstrated strong performance in classification problems and are suitable for predicting the discrete print-quality classes used in this study [38, 41, 44, 54-57]. Additionally, these ML models represent different levels of complexity and assumptions, allowing us to better evaluate trade-offs among predictive performance, model complexity, interpretability, and the ability to capture linear and nonlinear relationships in the dataset. **Table 4** compares the selected algorithms and highlights each model's main assumptions.

Table 4. Comparison between the selected ML models.

Group	**Models**	**Main characteristic/assumption**
Linear/discriminative	LR	Represents class boundaries using linear combinations of features; multinomial/one-vs-rest formulation must be stated [58].
Probabilistic/generative	GNB	Models continuous features using Gaussian class-conditional distributions; assumes conditional independence of features given the class [58].
Tree-based	CART	Recursive feature partitioning; captures nonlinear interactions without assuming linearity [58].
Ensemble tree-based	RF	Aggregates many decorrelated decision trees; robust to nonlinear interactions [58].
Kernel-based	SVM	Constructs a maximum-margin decision boundary; kernel functions such as RBF enable nonlinear classification; feature scaling is generally recommended [58].
Neural network	MLP	Learns nonlinear combinations of inputs through hidden layers; requires specification of architecture, activation, regularization, optimizer, etc [58].

The variables used by the ML models consisted of both pre-print condition variables and post-print measurements. The pre-print condition variables included bioink material (Pluronic F127 or Alg-Lap), feed rate, flow rate, and speed ratio. We also included geometry-specific post-print measurements because the ML framework aimed to screen printed construct quality rather than predict it from printer settings alone.

We performed all analysis in Python using Scikit-learn, with Pandas and NumPy for data handling and Matplotlib and Seaborn for visualization. All models used the library's default hyperparameters, except the MLP's maximum number of iterations, which we set to 1000 to ensure convergence. Model comparison was carried out using 3-fold stratified cross-validation with shuffling; cross-validation accuracy was computed with cross_val_score and reported as the mean and standard deviation across folds, and confusion matrices were computed from out-of-fold predictions obtained with cross_val_predict. Final evaluation was performed on a separately printed test batch.

2.5. Data processing and collection

We obtained data from different experiments run using a custom-built ITOP system. The biological constructs shown in the tables below are examples of each print quality class of 3D bioprinted data for both materials (Pluronic and Alg-Lap) under varying feed rate, flow rate, speed ratio, and construct parameters. Next, we conducted exploratory data analysis (EDA) as a data-preparation phase to check for errors and outliers in the dataset (see **Tables 5-8**). We evaluated missing values using descriptive statistics and a bar chart, identified outliers using a density plot, and then checked for highly correlated features.

Table 5. Snapshot of the crosshatch structure dataset.

Material	Feed rate	Flow rate	Pr	Broken pores	Filled pores	Pore area	Print quality
Pluronic	37.5	116	0	0	9	0	Bad
Alg-Lap	300	84	0	2	0	2.51	Bad
Pluronic	300	53	0.99	0	0	3.63	Okay
Alg-Lap	600	53	0.97	0	0	3.19	Okay
Pluronic	150	42	0.97	0	0	2.79	Best
Alg-Lap	600	336	0.92	0	0	1.68	Best

Table 6. Snapshot of the tubular structure dataset.

Material	Feed rate	Flow rate	Tube height	Tube width	Print quality
Pluronic	150	21	0.00	0.00	Bad

Alg-Lap	75	252	1.86	6.56	Bad
Pluronic	300	52	2.69	7.56	Okay
Alg-Lap	75	42	2.75	10.94	Okay
Pluronic	300	116	3.27	9.28	Best
Alg-Lap	300	84	2.52	9.51	Best

Table 7. Snapshot of the overhang data.

Material	Feed rate	Flow rate	Pass 1	Pass 2	Pass 3	Pass 4	Pass 5	Deflection 1	Deflection 2	Deflection 3	Deflection 4	Deflection 5	Print quality
Pluronic	75	42	0	1	1	1	1	0.00	1.42	0.44	0.20	0.11	Bad
Alg-Lap	75	336	0	0	0	0	0	0.00	0.00	0.00	0.00	0.00	Bad
Pluronic	600	168	1	1	1	1	1	1.60	0.25	0.17	0.17	0.17	Okay
Alg-Lap	150	116	1	1	1	1	1	1.75	0.71	0.48	0.27	0.11	Okay
Pluronic	75	21	1	1	1	1	1	0.80	0.41	0.27	0.17	0.10	Best
Alg-Lap	150	32	1	1	1	1	1	1.13	0.39	0.20	0.11	0.08	Best

Table 8. Snapshot of angular data

Material	Feed rate	Flow rate	Turn 1	Turn 2	Turn 3	Turn 4	Thickness	Print quality
Pluronic	37.5	21	1	1	1	0	1.82	Bad
Alg-Lap	150	84	1	1	1	0	1.92	Bad
Pluronic	300	21	1	1	1	1	0.60	Okay
Alg-Lap	300	42	1	1	1	1	0.87	Okay
Pluronic	75	32	1	1	1	1	1.49	Best
Alg-Lap	600	200	1	1	1	1	1.40	Best

2.6. Performance measures

A 3x3 confusion matrix was used to measure classification performance by comparing the actual class with the predicted class. This metric provides a detailed analysis of how well a model classifies instances into different categories. The model evaluation methods included accuracy, balanced accuracy, precision, recall, and F1-score to assess the classification model's performance. They are calculated as follows:

$$Accuracy = \frac{TP}{TP+TN+FP+FN} \quad \text{(IV)}$$

$$Balanced\ accuracy = \frac{1}{K}\sum_{i=1}^{k} Recall_i \quad \text{(V)}$$

$$Precision = \frac{TP}{TP+FP} \quad \text{(VI)}$$

$$Recall = \frac{TP}{TP+FN} \quad \text{(VII)}$$

$$F1 - score = 2\frac{Precision\ x\ Recall}{Recall+Precision} \quad \text{(VIII)}$$

where:

TP (True Positives) is the number of instances that were correctly classified as positive.
TN (True Negatives) is the number of instances that were correctly classified as negative.
FP (False Positives) is the number of instances that were incorrectly classified as positive.
FN (False Negatives) is the number of instances that were incorrectly classified as negative.

Finally, an AUC-ROC curve measures classification model performance at different threshold settings. It evaluates a classification model's ability to distinguish between positive and negative classes at different classification thresholds. Three ROC curves were generated for the "Bad", "Okay", and "Best" classes. For each class, we calculated the AUC separately. The AUC value for each class represents the degree to which the model distinguishes that class from others. Higher AUC values indicate the model distinguishes that class better from others. Alternatively, a lower AUC value indicates the model has trouble separating that class from the rest. We also assessed the model's overall performance by calculating micro- or macro-averaged AUC. With macro-averaging, we calculate each class's performance metric and then take the arithmetic mean across all classes. As a result, macro-averaging gives every class the same weight. In contrast, micro-averaging sums true positives, false positives, and false negatives across all classes before calculating the performance metric. Thus, micro-averaging weights each instance equally, regardless of class label or instance count.

3. Results

Figure 4 shows accuracies for a combination of bioink types (Pluronic and Alg-Lap). The performance of the models was also evaluated using a confusion matrix and an AUC-ROC curve as seen in **Figures 5-12**. The results showed that bioink type significantly influenced bioprinted construct quality, with certain bioinks yielding better outcomes than others. The ML models showed promising predictive capabilities, accurately estimating bioprinted construct quality based on bioink type, printing process parameters, and bioprinted structure. These findings highlight the potential of ML algorithms to optimize bioprinting processes by guiding bioink selection for improved bioprinted construct quality.

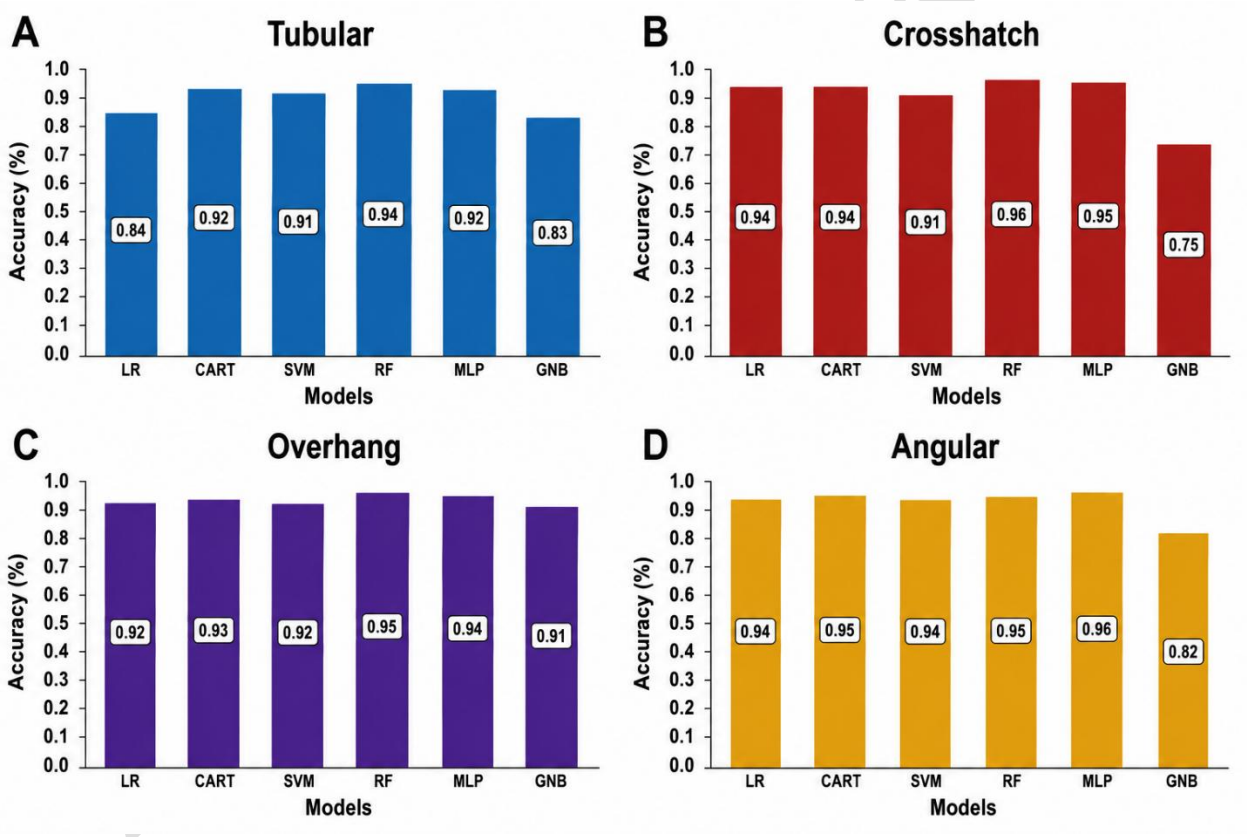

Figure 4. ML model accuracy values for (a) tubular structure; (b) crosshatch structure; (c) overhang structure; and (d) angular structure.

3.5. Tubular structure

The results for the best (RF) and least (GNB) performing models are presented for the tubular structure. The RF model demonstrated a very strong overall performance, particularly in identifying "Bad" prints. As shown in **Figure 5a**, 9 "Best" prints were incorrectly classified as "Okay," while none were classified as "Bad." Among the "Okay" prints, 4 were misclassified as "Best" and 5 as "Bad." Of the "Bad" prints, only 1 was misclassified as "Best" and 1 as "Okay." These results indicate that most misclassifications occurred between the "Best" and "Okay" classes, suggesting that further feature selection and model tuning may improve discrimination between these print-quality categories. The AUC-ROC results (**Figure 5b**) demonstrated excellent discriminatory performance, with AUC values of 0.99, 0.98, and 1.00 for the "Best," "Okay," and "Bad" classes, respectively. The micro-average and macro-average AUC values were both 0.99.

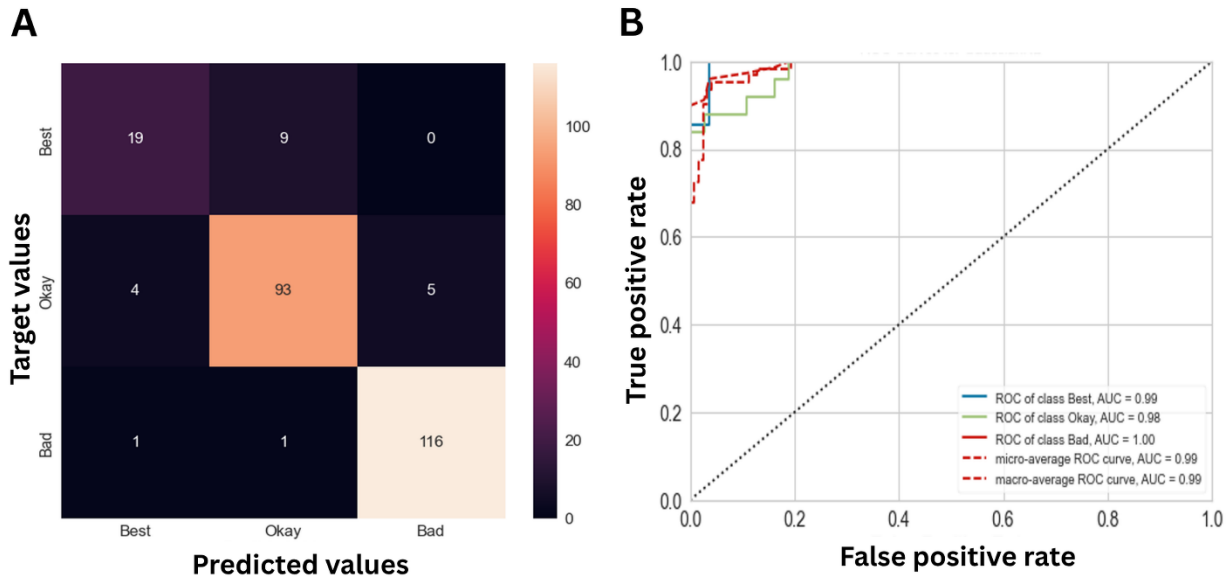

Figure 5. (a) RF confusion matrix results, and (b) AUC-ROC results for the tubular structure.

The RF model achieved an overall classification accuracy of 91.9% and balanced accuracy of 85.8%, with weighted precision, weighted recall, weighted F1-score, and macro-F1 values of 0.917, 0.919, 0.918, and 0.870, respectively (**Table 9**). Class-specific performance was highest for the "Bad" (F1-score = 0.971) and "Okay" (F1-score = 0.907) classes, whereas the "Best" class

showed comparatively lower performance (F1-score = 0.731), primarily due to its lower recall (0.679).

Table 9. Classification performance metrics of the best (RF) and least (GNB) performing models for quality print prediction.

Model	**Accuracy**	**Balanced accuracy**	**Weighted precision**	**Weighted recall**	**Macro-F1**	**Weighted F1-score**
RF	0.919	0.858	0.917	0.919	0.870	0.917
GNB	0.843	0.828	0.851	0.843	0.813	0.845

As shown in **Figure 6a**, the GNB model misclassified 5 "Best" prints as "Okay" and 1 as "Bad." The model also showed difficulty classifying "Okay" prints, with 10 misclassified as "Best" and 6 as "Bad". Among the "Bad" prints, 16 were misclassified as "Okay" and 1 as "Best." Overall, the model showed the highest recall for the "Bad" class (85.6%), followed by "Okay" (84.3%) and "Best" (78.6%). The AUC-ROC results shown in **Figure 6b** further demonstrate the model's ability to discriminate among the three print-quality classes. It had AUC values of 0.91, 0.96, and 0.97 for "Best", "Okay", and "Bad" classes, respectively. The micro-average ROC score was 0.97, and the macro-average ROC score was 0.95.

The GNB model achieved an overall classification accuracy of 84.3% and balanced accuracy of 82.8, with weighted precision, weighted recall, weighted F1-score, and macro-F1 values of 0.851, 0.843, 0.845, and 0.813, respectively (**Table 9**). Class-specific performance was highest for the "Bad" (F1-score = 0.893), followed by "Okay" (F1-score = 0.823) classes, and the "Best" class

with lower performance (F1-score = 0.721), primarily due to its lower precision (0.667).

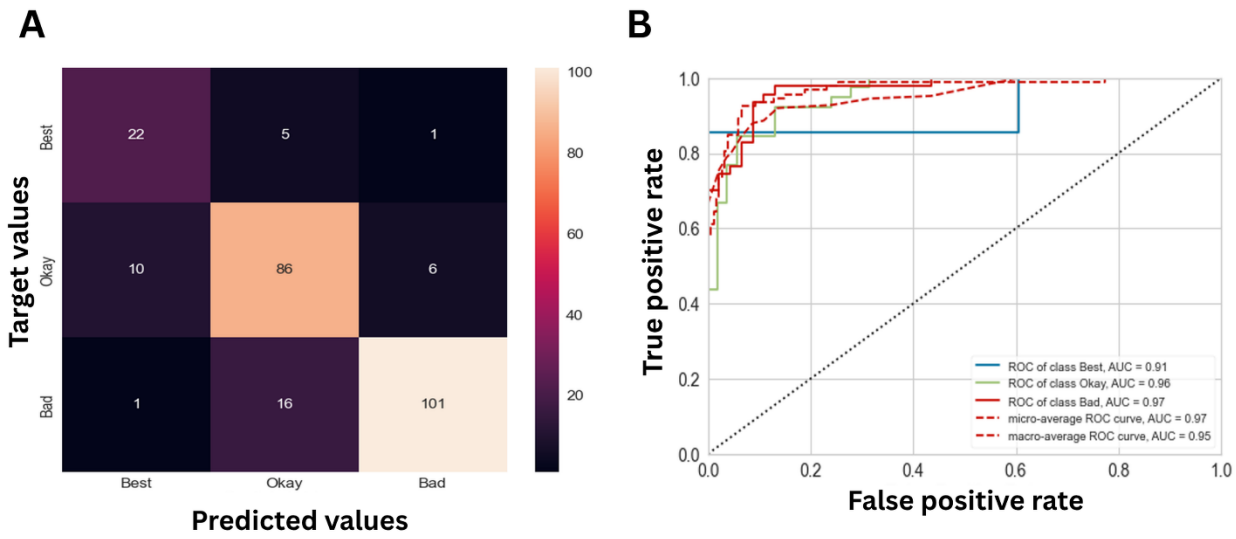

Figure 6. a). GNB confusion matrix results, and b). AUC-ROC results for the tubular structure.

We also tested the models on an external dataset not used during training, and **Table 10** presents examples of the testing classification sample results for the best model (RF). This helps ensure the models generalize to new data. Thus, our models can accurately evaluate input conditions for a desired outcome. The images in the "Print outcome" column support this assessment by clearly showing the structural integrity and resolution of each print. Both bioinks produced optimal results under specific conditions, as evidenced by the sharpness and absence of defects in the corresponding images for quality "Best". Conversely, a decline in these factors corresponds to a lower quality rating, illustrating the importance of precise parameter control in bioprinting processes.

Table 10. Tubular structure testing outcome for the best ML model (RF).

Material	Feed rate (mm/min)	Flow rate (mm^3/min)	Tube height (mm)	Tube width (mm)	RF ML classified quality	Print outcome

Pluronic	75	37.5	3.77	9.52	Best	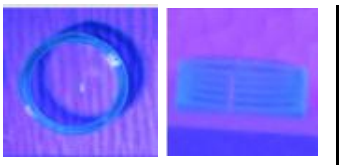
Alg-Lap	37.5	21	2.76	9.48	Best	
Pluronic	75	84	3.5	8.86	Okay	
Alg-Lap	600	168	2.43	9.78	Okay	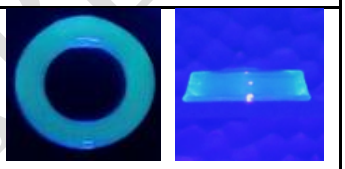
Pluronic	75	168	2.56	7.13	Okay	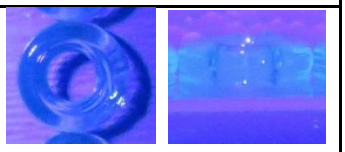
Pluronic	150	21	0	0	Bad	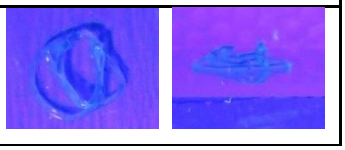

3.6. Crosshatch structure

The results for the best (RF) and least (GNB) performing models are presented for the crosshatch structure. The RF crosshatch confusion matrix shows that only two "Best" prints were misclassified as "Okay" and "Bad," respectively (Figure 7a), while the remaining "Best" prints were correctly classified. Furthermore, three "Okay" prints were misclassified as "Best," and two "Okay" prints were misclassified as "Bad". For the "Bad" prints, two were misclassified as "Best" and another two were misclassified as "Okay". The model's AUC-ROC results (**Figure 7b**) further demonstrated strong discriminatory performance, with AUC values of 0.99, 0.97, and 0.99 for the "Best", "Okay", and "Bad" classes, respectively. The micro-average ROC score was 0.99, and the macro-average ROC score was 0.99.

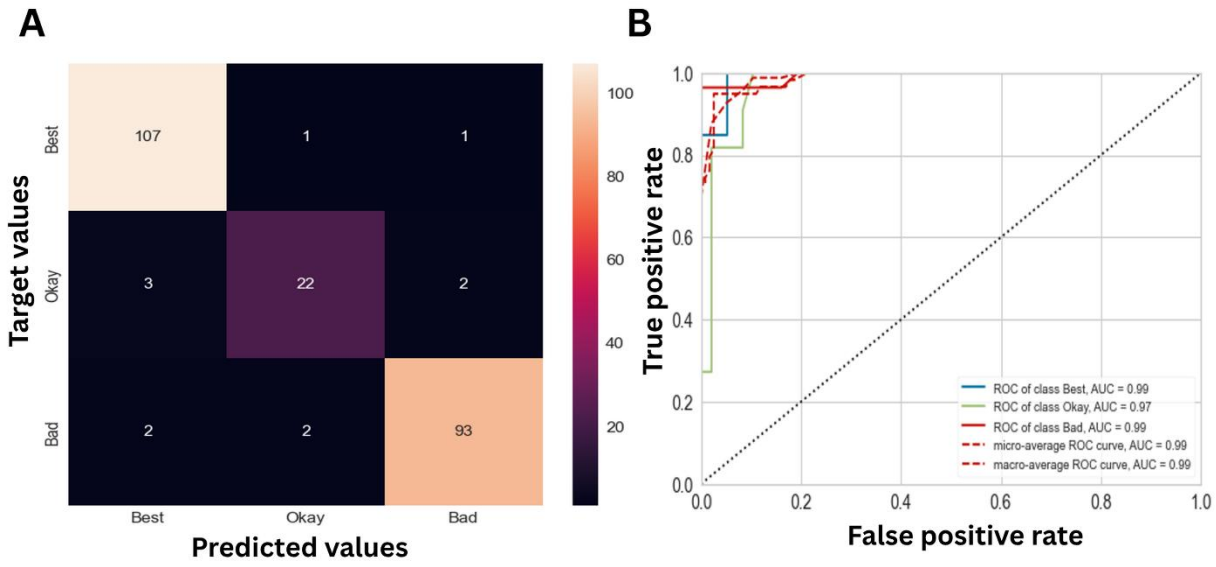

Figure 7. a) RF confusion matrix and b) AUC-ROC results for the crosshatch structure.

The RF model achieved an overall classification accuracy of 95.3% and balanced accuracy of 91.8%, with weighted precision, weighted recall, weighted F1-score, and macro-F1 values of 0.952, 0.953, 0.952, and 0.926, respectively (**Table 11**). Class-specific performance was highest for the Best (F1-score = 0.968) and Bad (F1-score = 0.964) classes, whereas the Okay class performed comparatively worse (F1-score = 0.846), primarily due to its lower recall (0.815).

Table 11. Classification performance metrics of the best (RF) and least (GNB) performing models for quality print prediction.

Model	Accuracy	Balanced accuracy	Weighted precision	Weighted recall	Macro-F1	Weighted F1-score
RF	0.953	0.918	0.952	0.953	0.926	0.952
GNB	0.751	0.783	0.854	0.751	0.704	0.769

For the GNB model, the confusion matrix in **Figure 8a** shows that the classifier performed best in identifying the "Bad" class, correctly classifying 90 instances, while 7 "Bad" prints were misclassified as "Okay." However, the model showed difficulty distinguishing between the "Best" and "Okay" classes. Specifically, 37 "Best" prints were misclassified as "Okay," whereas 4 "Okay" prints were misclassified as "Best." Additionally, 10 "Best" prints were misclassified as "Bad." Overall, the model showed the highest recall for the "Bad" class (92.8%), followed by "Okay" (85.2%) and "Best" (56.9%), and achieved an overall classification accuracy of 75.1%. The ROC curves provide a complementary perspective on model performance. The classifier achieved AUC values of 0.99, 0.98, and 0.96 for the "Best," "Okay," and "Bad" classes, respectively (**Figure 8b**). The micro-average and macro-average AUC values were 0.94 and 0.98, respectively, indicating strong overall discriminatory ability across classification thresholds despite the lower classification accuracy observed at the selected decision rule.

We also evaluated the GNB model's weighted precision, weighted recall, weighted F1-score, and macro-F1, obtaining values of 0.854, 0.751, 0.769, and 0.704, respectively (**Table 11**). Class-specific performance was highest for "Bad" (F1-score = 0.914), whereas "Best" (F1-score = 0.709) and "Okay" (F1-score = 0.489) showed comparatively lower performance, with very low precision for "Okay" (0.343).

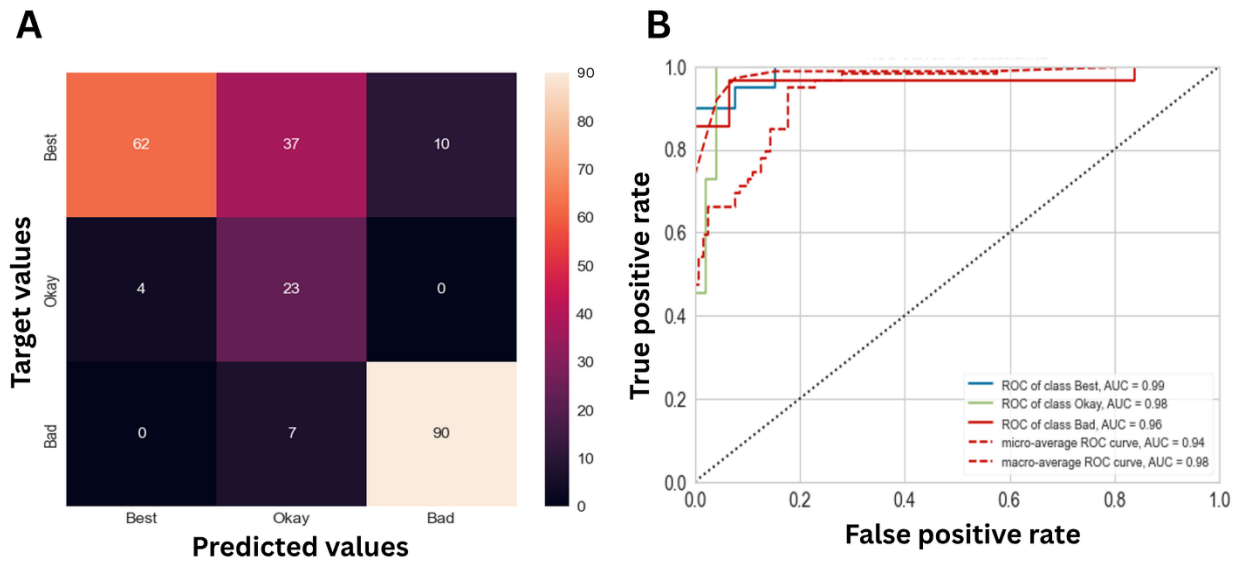

Figure 8. a) GNB confusion matrix, and b) AUC-ROC results for the crosshatch structure.

Because the RF algorithm was most accurate for crosshatch, we used its results to test structure quality on external data and compared the predictions with the actual print results. **Table 12** presents a few testing samples. For Pluronic, the RF's "Best" predictions were supported by images showing meticulously defined crosshatch patterns. As parameters such as flow rate varied, the algorithm predicted a decline in quality to "Okay" and then to "Bad", consistent with the observed structural imperfections in the physical prints. Alg-Lap also exhibited similar results, with "Best" predictions aligning with high-quality print results. The RF algorithm's accurate performance in predicting the quality of these intricate structures underscores its utility in optimizing bioprinting for complex geometric patterns like crosshatches.

Table 12. Crosshatch structure testing outcome for the best ML model (RF)

Material	Feed rate (mm/min)	Flow rate (mm^3/min)	Pr value	Broken pores	Filled pores	Area of pores (mm^2)	RF ML classified quality	Print outcome
Pluronic	150	84	0.99	0	0	1.98	Best	
Alg-Lap	600	336	0.95	0	0	1.91	Best	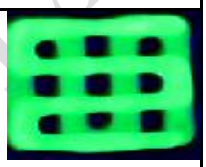
Pluronic	300	42	0.99	0	0	4.01	Okay	
Pluronic	37.5	84	0	0	9	0	Bad	
Alg-Lap	150	21	0	8.67	0	0	Bad	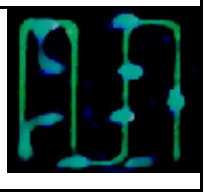

3.7. Angular structure

The results for the best-performing (MLP) and least-performing (GNB) models are presented for the angular structure. **Figure 9a** shows that the MLP predicted the classes “Bad”, “Okay”, and “Best” with high accuracy. The confusion matrix shows that out of 194 instances labeled “Bad”, only 2 were misclassified as “Okay”. For the “Okay” class, 22 of 28 instances were correctly identified, while three were misclassified as “Best” and three as “Bad”. The model also correctly classified 19 of the 20 “Best” prints, with only 1 misclassified as “Okay.” The model showed the highest recall for the “Bad” class (99.0%), followed by the “Best” (95.0%) and “Okay” (78.6%) classes, indicating comparatively greater difficulty in correctly identifying “Okay” prints. The

ROC curves (**Figure 9b**) provide a complementary assessment of the model's discriminatory performance, with AUC values of 0.99, 0.86, and 0.97 for “Best”, “Okay”, and “Bad”, respectively.

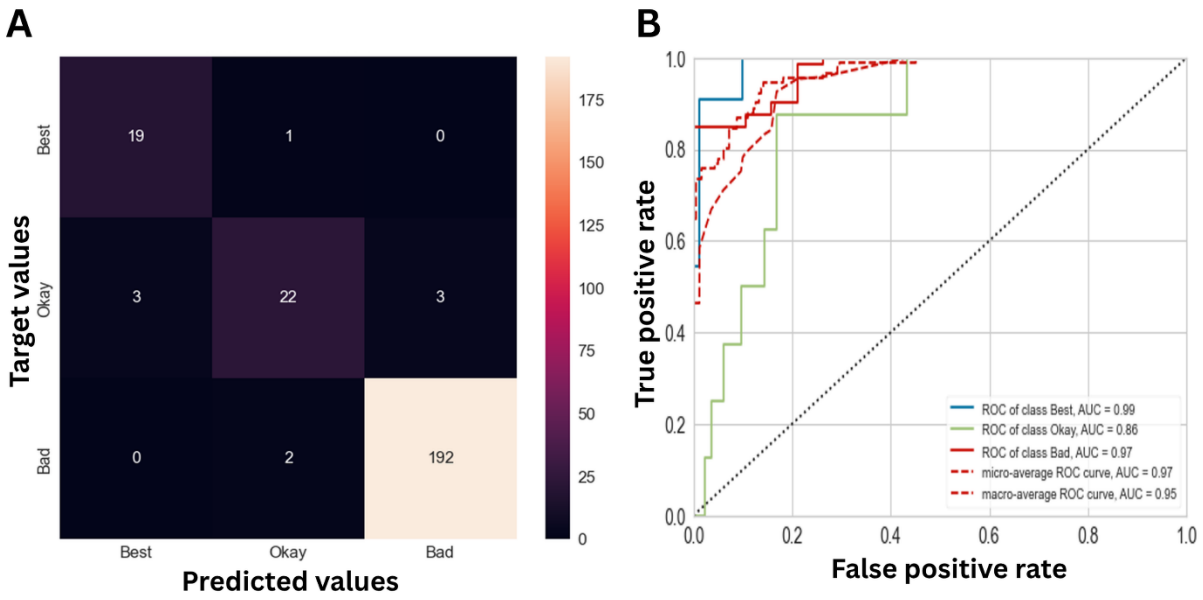

Figure 9. a) MLP confusion matrix results, and b). AUC-ROC results for the angular structure.

We also evaluated the MLP model’s weighted precision, weighted recall, weighted F1-score, and macro-F1, obtaining values of 0.963, 0.963, 0.962, and 0.907, respectively (**Table 13**). The model achieved an accuracy of 96.3% and balanced accuracy of 90.8%. Class-specific performance was highest for “Bad” (F1-score = 0.987), followed by “Best” (F1-score = 0.905) and “Okay” (F1-score = 0.830).

Table 13. Classification performance metrics of the best (MLP) and least (GNB) performing models for quality print prediction.

Model	**Accuracy**	**Balanced Accuracy**	**Weighted precision**	**Weighted recall**	**Macro-F1**	**Weighted F1-score**
MLP	0.963	0.908	0.963	0.963	0.907	0.962
GNB	0.822	0.697	0.865	0.822	0.608	0.835

The GNB classifier demonstrated high recall for the "Best" class, correctly identifying 19 of 20 "Best" prints, with only 1 misclassified as "Okay" (**Figure 10a**). However, the model struggled to identify the "Okay" class, correctly classifying only 7 of 28 instances; it misclassified 20 as "Best" and one as "Bad." For the "Bad" class, 173 of 194 prints were correctly classified, while 20 were misclassified as "Okay" and 1 as "Best." Overall, the model achieved 82.23% accuracy and a balanced accuracy of 69.7% (**Table 13**). The ROC curves (**Figure 10b**) showed AUC values of 0.83, 0.83, and 1.00 for the "Best," "Okay," and "Bad" classes, respectively. The micro-average and macro-average AUC values were 0.95 and 0.90, respectively, indicating strong overall discriminatory ability, although discrimination was considerably better for the "Bad" class than for the "Best" and "Okay" classes. Notably, the "Bad" class achieved an AUC of 1.00 despite some misclassifications in the confusion matrix. This difference arises because AUC evaluates the model's ability to rank or discriminate a class across all possible classification thresholds, whereas the confusion matrix reflects the final class assignments at a specific decision rule.

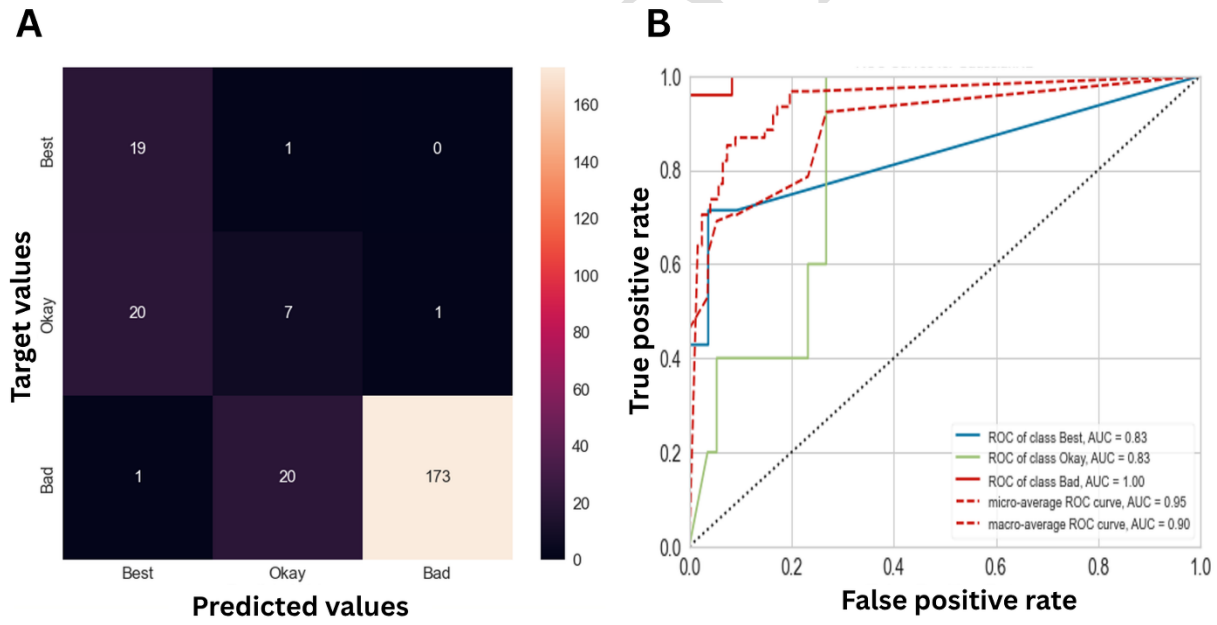

Figure 10. a) GNB confusion matrix results, and b). AUC-ROC results for the angular structure

We also evaluated the GNB model's weighted precision, weighted recall, weighted F1-score, and macro-F1, obtaining values of 0.865, 0.822, 0.835, and 0.608, respectively (**Table 13**). Class-

specific performance was highest for “Bad” (F1-score = 0.940), whereas “Best” (F1-score = 0.633) and “Okay” (F1-score = 0.250) showed comparatively lower performance.

Table 14 presents the testing results for the angular structure**.** We selected the MLP algorithm for testing because it performed better than other candidate models. We then compared the algorithm's predictions with actual angular print outcomes. For instance, when the MLP algorithm predicted a bioprinted construct quality of “Best”, this was expected to align with prints that exhibited high precision and a flawless structure. When actual prints matched the algorithm’s good-quality prediction, this underscored its ability to interpret and predict outcomes based on the printing parameters fed into it. The algorithm also performed well on prints assigned quality levels “Okay” and “Bad”. These predictions corresponded to printed constructs with varying differences in thickness (filament width) and turn sharpness. The MLP algorithm successfully captured these variations; it identified the drop to “Bad” associated with more challenging parameter settings, such as higher feed rates, which was validated by flaws in the physical prints. In addition, for “Okay” predictions, the actual prints showed intermediate quality between “Best” and “Bad”, demonstrating the algorithm's ability to differentiate between print-quality levels. This level of detail in the MLP algorithm's predictions validates its effectiveness and reinforces its selection as an accurate tool for assessing bioink printability.

Table 14. Angular structure testing outcome for the best ML model (MLP).

Material	Feed rate (mm/min)	Flow rate (mm^3/min)	Turn				Thickness (mm)	MLP ML classified quality	Print outcome
			1	2	3	4			
Pluronic	75	21	1	1	1	1	1.43	Best	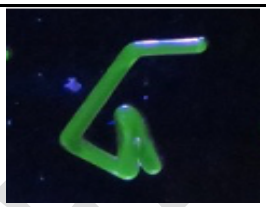
Alg-Lap	600	84	1	1	1	1	0.75	Okay	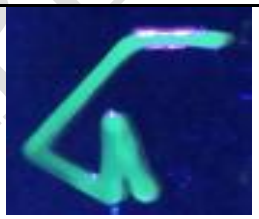
Alg-Lap	600	21	1	1	1	1	0.49	Okay	
Alg-Lap	75	84	1	0	0	0	0	Bad	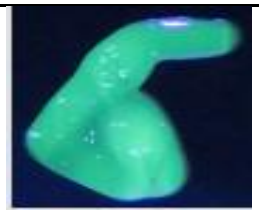
Pluronic	300	168	1	1	0	0	1.66	Bad	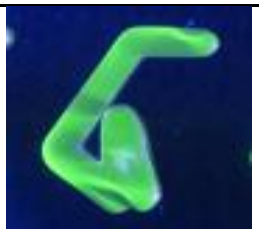

3.8. Overhang structure

The RF classifier showed strong overall classification performance (**Figure 11a**), achieving 96.0% accuracy and 86.9% balanced accuracy. The confusion matrix shows that the classifier correctly identified 15 of the 20 “Best” prints but misclassified 5 as “Okay.” For the “Okay” class, 25 of 29

prints were correctly identified, while four were misclassified as “Best.” The model performed best on the “Bad” class, correctly identifying 198 of 199 prints, with only one misclassified as “Okay.” The ROC curves (**Figure 11b**) further demonstrated strong discriminatory performance, with AUC values of 0.98, 0.97, and 1.00 for the “Best,” “Okay,” and “Bad” classes, respectively. These results indicate that the RF model strongly discriminated among the three print-quality classes, with particularly strong performance for the “Bad” class.

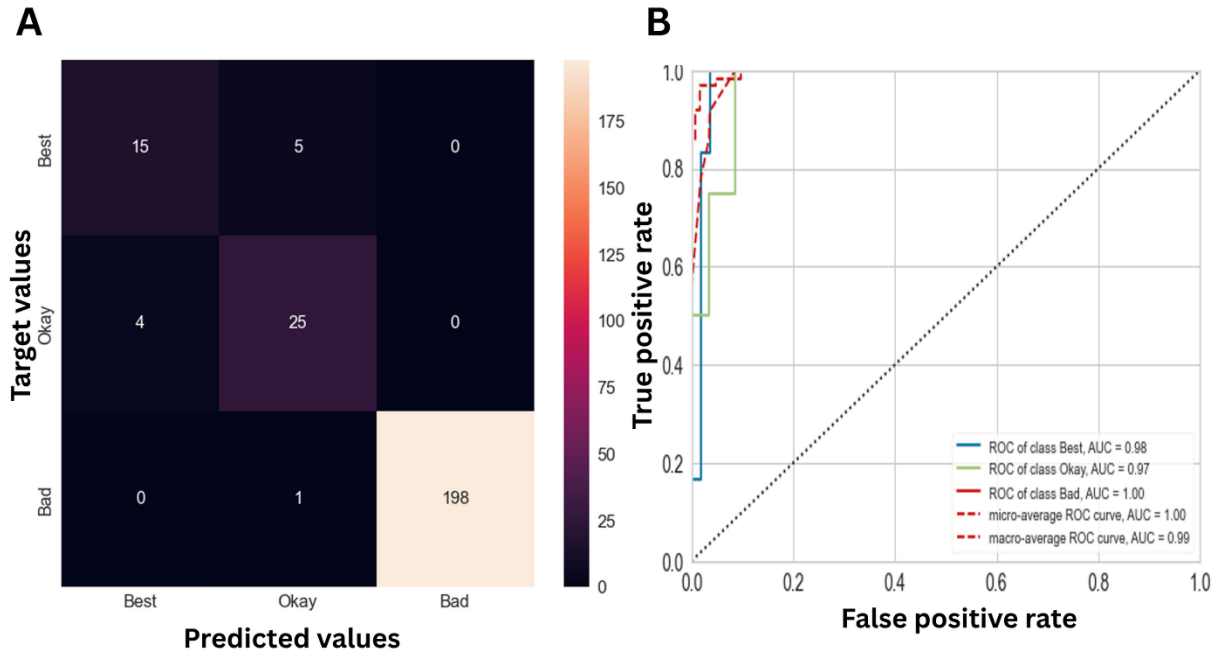

Figure 11. a) RF confusion matrix results, and b) AUC-ROC results for the overhang structure.

Table 15 presents the classification performance metrics for the overhang structure for the RF model: weighted precision, weighted recall, weighted F1-score, and macro-F1, with values of 0.960, 0.960, 0.960, and 0.867, respectively. Class-specific performance was highest for “Bad” (F1-score = 0.997), whereas “Best” (F1-score = 0.833) and “Okay” (F1-score = 0.769) showed slightly lower performance.

Table 15. Classification performance metrics of the best (RF) and least (GNB) performing models for quality print prediction.

Model	Accuracy	Balanced accuracy	Weighted precision	Weighted recall	Macro-F1	F1-score
RF	0.960	0.869	0.960	0.960	0.867	0.960
GNB	0.911	0.710	0.912	0.911	0.709	0.912

The GNB confusion matrix results (**Figure 12a**) show that the classifier achieved an overall accuracy of 91.1%, but performance was inconsistent across the three print-quality classes, as reflected in the lower balanced accuracy (71.1%). Of the 20 "Best" prints, 11 were correctly classified, while 9 were misclassified as "Okay." For the "Okay" class, 17 of 29 prints were correctly classified, while 11 were misclassified as "Best" and one as "Bad." The model performed best on the "Bad" class, correctly classifying 198 of 199 prints, with only one misclassified as "Okay." The model achieved recall values of 55.0%, 58.6%, and 99.5% for the "Best," "Okay," and "Bad" classes, respectively. The ROC curves (**Figure 12b**) showed AUC values of 0.96, 0.83, and 1.00 for the "Best," "Okay," and "Bad" classes, respectively. The micro-average and macro-average AUC values were 0.98 and 0.93, respectively. These results indicate excellent discriminatory ability for the "Bad" class, while the lower AUC for the "Okay" class suggests greater difficulty discriminating this class across classification thresholds.

We also evaluated the GNB model's weighted precision, weighted recall, weighted F1-score, and macro-F1 values, obtaining values of 0.912, 0.911, 0.912, and 0.709, respectively (**Table 15**). Class-specific performance was highest for the "Bad" class (F1-score = 0.995), whereas substantially lower performance was observed for the "Okay" (F1-score = 0.607) and "Best" (F1-score = 0.524) classes, indicating greater difficulty in correctly distinguishing these print-quality categories.

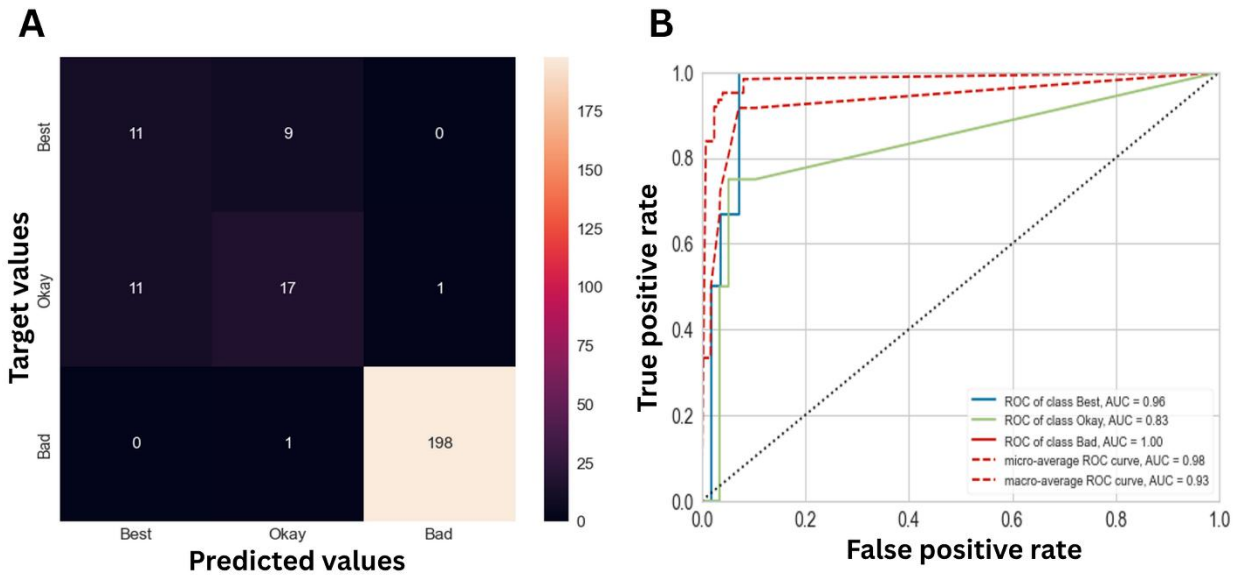

Figure 12. a). GNB confusion matrix results, and b). AUC-ROC results for the overhang structure.

As shown in **Table 16**, we tested the overhang structure results by comparing RF print-quality results with images of actual print or construct outcomes to assess their efficacy in a practical scenario. We selected the RF model because it outperformed the other models. It accurately forecasted print quality levels. The "Pass" and "Deflection" columns represent quantifiable aspects of overhang structures' print quality. The results show that the RF's "Best" prints were validated by the associated images, which showed precise deflection at the midpoint and smooth transitions between gaps. Similarly, the RF predictions of "Okay" and "Bad" aligned with images of prints showing significant flaws and print-quality inconsistencies, illustrating a correlation between the RF's predictions and actual print defects. The RF's ability to discern complex interactions between print parameters and their impact on print outcome demonstrates its usefulness in enhancing the 3D printing process through intelligent, adaptive quality assessment.

Table 16. Overhang structure testing outcome for the best ML model (RF).

Material	Feed rate (mm/min)	Flow rate (mm^3/min)	Pass					Deflection (mm)					RF ML classified quality	Print outcome
			1	2	3	4	5	1	2	3	4	5		
Pluronic	75	21	1	1	1	1	1	0.80	0.41	0.27	0.17	0.10	Best	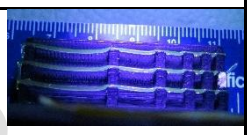
Alg-Lap	300	168	1	1	1	1	1	1.58	0.55	0.32	0.17	0.08	Best	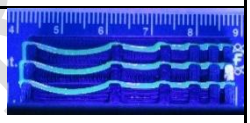
Alg-Lap	75	42	1	1	1	1	1	2.42	0.48	0.22	0.09	0.07	Okay	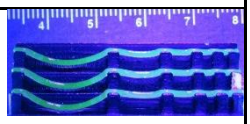
Pluronic	37.5	336	0	0	0	0	0	0	0	0	0	0	Bad	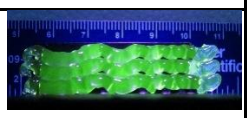
Alg-Lap	600	84	0	1	1	1	1	0	0.24	0.23	0.16	0.04	Bad	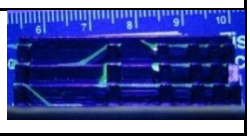

4. Discussion

Model performance differed across the four bioprinted constructs, indicating that classifier suitability depended on structure. RF achieved the highest accuracy for tubular (91.9%; balanced accuracy 85.8%), crosshatch (95.3%; balanced accuracy 91.8%), and overhang (96.0%; balanced accuracy 86.9%) structures, while MLP performed best for the angular structure (96.3%; balanced accuracy 90.8%). RF therefore provided the most consistently strong performance across geometries, whereas MLP was particularly effective for the angular structure. Angular structures are often challenging because they require high bioink structural integrity and fine resolution at sharp angles and intersections. The MLP's architecture enables it to model complex relationships and interactions. Accurate modeling of complex constructs, such as angular structures, indicates its potential to optimize bioink printing parameters for challenging geometries.

GNB's comparatively weaker performance, particularly for the “Okay” class in several geometries, may relate to its underlying assumptions and the nature of the data. In GNB, features are assumed to be normally distributed. The presence (or absence) of a feature is independent of the presence

(or absence) of any other feature given the class variable. In this case, good performance may be achieved if the features approximate these assumptions or if their deviations are not significant. The confusion matrices show that errors frequently occurred between adjacent quality categories, especially “Best” and “Okay,” suggesting overlap near the threshold-based class definitions. The high AUC values for some GNB models, despite lower class-assignment accuracy, are not contradictory: AUC evaluates ranking across thresholds, whereas the confusion matrix reflects the final multiclass decision rule.

By contrast, the LR model's poor performance on tubular structure stems from its linear assumption that outcomes are predicted as a linear combination of input features. While LR is robust and effective when the relationship between input variables and the output is approximately linear, it struggles when this relationship is highly nonlinear, as is often the case in bioprinting. Overall, the findings highlight the critical role of model selection in evaluating bioprinting outcomes.

RF’s overall high accuracy reflects its potential as a reliable predictive tool in a variety of bioprinting scenarios. Furthermore, the MLP's strong performance on angular structures highlights neural networks' potential to improve bioprinting precision and reliability. This is especially important because accurately replicating complex geometries is crucial to creating functional biological structures.

Bioprinting involves non-linear dynamics, where interactions between printing parameters and bioink properties can nonlinearly affect printed-structure quality. ML is essential for advancing bioprinting technologies, enabling more precise and accurate tissue and organ printing. Key areas where ML can improve bioprinting include: 1) Biomaterial Development: Bioprinting requires specialized biomaterials that can support cell growth and tissue formation [59]. Developing these materials is time-consuming, costly, and often trial-and-error-based. Applying ML to bioprinting can accelerate biomaterial development by predicting mechanical and biological properties and identifying new combinations that may improve tissue formation. 2) Cell Behavior Modeling: Bioprinting involves the deposition of living cells onto a scaffold in a controlled manner to create a 3D structure[60]. However, cell behavior is complex and difficult to predict. ML can model cell behavior, understand cell interactions with other cells and their environment, and optimize printing to produce more accurate and reproducible tissue constructs. 3) Cell Viability: It can help fine-tune bioprinting conditions by analyzing critical process parameters like UV intensity, exposure

time, bioink composition, and layer thickness, thereby optimizing conditions for enhanced cell survival [61].

5. Conclusion

Exploring predictive modeling algorithms such as MLP, RF, SVM, GNB, CART, and LR marks a significant advancement in bioprinting. In this study, these algorithms have been used to forecast bioprinted construct quality outcomes using Pluronic and Alg-Lap bioinks across four bioprinted structures. The algorithms offer a diverse range of approaches, from the simplicity and interpretability of LR to the complex, nonlinear capabilities of MLP, each bringing unique strengths to the prediction task. Using these algorithms to predict bioprinted construct quality is crucial because the bioprinting process involves complex interactions among parameters and the inherent properties of bioinks, which significantly influence final structure quality. The present work revealed key insights: RF emerged as the best-performing model overall, achieving 85.8%, 91.8%, and 86.9% balanced accuracies for the tubular, crosshatch, and overhang structures, respectively. MLP performed best for the angular structure, with an accuracy of 90.8%. GNB was the least effective, achieving balanced accuracies of 82.8%, 78.3%, 71.0%, and 69.7% for the tubular, crosshatch, overhang, and angular structures, respectively. This performance gap can be attributed to the inherent characteristics of these algorithms and the complex nature of bioprinting data. The superior performance of RF and MLP algorithms can be attributed to their sophisticated mechanisms for learning from and adapting to the complex, multidimensional data associated with bioprinting processes. These models' ability to navigate the intricate relationships between printing parameters and bioprinted construct quality outcomes underscores the importance of selecting appropriate predictive modeling techniques that align with the data's nature. Conversely, the underperformance of GNB and LR highlights the challenges of applying models with simplistic assumptions to complex, real-world problems, reaffirming the need to carefully consider algorithmic suitability in predictive modeling endeavors. By enabling prediction of bioprinted construct quality outcomes before printing, these models significantly reduce material waste, save time, and increase the likelihood of producing bioprinted structures that meet desired specifications and functional requirements. This predictive approach represents a paradigm shift in bioprinting, moving towards a more data-driven, personalized fabrication process that holds promise for advancing tissue engineering and regenerative medicine applications.

Acknowledgments

None.

Funding

The authors would like to express their gratitude for funding support from the National Science Foundation Grant (NSF Engines Award #2315654).

Conflict of interest

The authors declare no conflict of interest. The funders had no role in the design of the study; in the collection, analyses, or interpretation of data; in the writing of the manuscript, or in the decision to publish the results.

Author contributions

Conceptualization: All authors
Formal analysis: Joan Isichei, Siyuan Li, Izabele Heyward
Funding acquisition: Salil Desai, Sang Jin Lee
Investigation: All authors
Methodology: Joan Isichei, Siyuan Li, Joshua Copus, Izabele Heyward
Supervision: Sang Jin Lee, Izabele Heyward, Salil Desai
Writing–original draft: Joan Isichei, Siyuan Li, Izabele Heyward

Ethics approval and consent to participate

Not applicable.

Consent for publication

Not applicable.

Availability of data

The data presented in this study are available on request from the corresponding author.

Further disclosure

During the preparation of this manuscript, the authors used Microsoft Copilot (Microsoft Corporation, Redmond, WA, USA), powered by OpenAI's GPT-4/GPT-4 Turbo models, to assist with manuscript conceptualization, language editing, grammar checking, and improving the text's clarity and readability. The AI tools were not used to generate or interpret scientific data or perform analyses. All AI-assisted content was critically reviewed, edited, and verified by the authors. The authors accept full responsibility for the accuracy, integrity, and originality of the manuscript and confirm that all cited information and scientific content were independently verified.

References

1. Murphy SV, De Coppi P, Atala A. Opportunities and challenges of translational 3D bioprinting. Nat Biomed Eng. 2020;4(4):370-380. doi:10.1038/s41551-019-0471-7
2. Mao H, Yang L, Zhu H, et al. Recent advances and challenges in materials for 3D bioprinting. Prog Nat Sci Mater Int. 2020;30(5):618-634. doi:10.1016/j.pnsc.2020.09.015
3. Fang Y, Guo Y, Liu T, et al. Advances in 3D bioprinting. Chin J Mech Eng Addit Manuf Front. 2022;1(1):100011. doi:10.1016/j.cjmeam.2022.100011
4. Matai I, Kaur G, Seyedsalehi A, McClinton A, Laurencin CT. Progress in 3D bioprinting technology for tissue/organ regenerative engineering. Biomaterials. 2020;226:119536. doi:10.1016/j.biomaterials.2019.119536
5. Schwab A, Levato R, D'Este M, Piluso S, Eglin D, Malda J. Printability and shape fidelity of bioinks in 3D bioprinting. Chem Rev. 2020;120(19):11028-11055. doi:10.1021/acs.chemrev.0c00084
6. Zhang YS, Haghiashtiani G, Hübscher T, et al. 3D extrusion bioprinting. Nat Rev Methods Primers. 2021;1(1):75. doi:10.1038/s43586-021-00073-8

7. Ji S, Guvendiren M. Complex 3D bioprinting methods. APL Bioeng. 2021;5(1):011508. doi:10.1063/5.0034901
8. Cui X, Li J, Hartanto Y, et al. Advances in extrusion 3D bioprinting: a focus on multicomponent hydrogel-based bioinks. Adv Healthc Mater. 2020;9(15):e1901648. doi:10.1002/adhm.201901648
9. Weng T, Zhang W, Xia Y, et al. 3D bioprinting for skin tissue engineering: current status and perspectives. J Tissue Eng. 2021;12:20417314211028574. doi:10.1177/20417314211028574
10. Gungor-Ozkerim PS, Inci I, Zhang YS, Khademhosseini A, Dokmeci MR. Bioinks for 3D bioprinting: an overview. Biomater Sci. 2018;6(5):915-946. doi:10.1039/C7BM00765E
11. Gopinathan J, Noh I. Recent trends in bioinks for 3D printing. Biomater Res. 2018;22:11. doi:10.1186/s40824-018-0122-1
12. Donderwinkel I, Van Hest JCM, Cameron NR. Bio-inks for 3D bioprinting: recent advances and future prospects. Polym Chem. 2017;8(31):4451-4471. doi:10.1039/C7PY00826K
13. Chimene D, Lennox KK, Kaunas RR, Gaharwar AK. Advanced bioinks for 3D printing: a materials science perspective. Ann Biomed Eng. 2016;44(6):2090-2102. doi:10.1007/s10439-016-1638-y
14. Lee JM, Yeong WY. Design and printing strategies in 3D bioprinting of cell-hydrogels: a review. Adv Healthc Mater. 2016;5(22):2856-2865. doi:10.1002/adhm.201600435
15. Jose RR, Rodriguez MJ, Dixon TA, Omenetto FG, Kaplan DL. Evolution of bioinks and additive manufacturing technologies for 3D bioprinting. ACS Biomater Sci Eng. 2016;2(10):1662-1678. doi:10.1021/acsbiomaterials.6b00088
16. Parupelli SK, Saudi S, Bhattarai N, Desai S. 3D printing of PCL-ceramic composite scaffolds for bone tissue engineering applications. Int J Bioprint. 2023;9(6):0196. doi:10.36922/ijb.0196
17. Ogunsanya M, Desai S. Physics-based and data-driven modeling for biomanufacturing 4.0. Manuf Lett. 2023;36:91-95. doi:10.1016/j.mfglet.2023.04.003
18. Tettey F, Saudi S, Davies D, et al. Fabrication and characterization of Zn particle incorporated fibrous scaffolds for potential application in tissue healing and regeneration. ACS Appl Mater Interfaces. 2023;15(42):48913-48929. doi:10.1021/acsami.3c09793

19. Adarkwa E, Roy A, Ohodnicki J, Desai S. 3D printing of drug-eluting bioactive multifunctional coatings for orthopedic applications. Int J Bioprint. 2023;9(2):661. doi:10.18063/ijb.v9i2.661
20. Lee SC, Gillispie G, Prim P, Lee SJ. Physical and chemical factors influencing the printability of hydrogel-based extrusion bioinks. Chem Rev. 2020;120(19):10834-10886. doi:10.1021/acs.chemrev.0c00015
21. Gillispie G, Prim P, Copus J, et al. Assessment methodologies for extrusion-based bioink printability. Biofabrication. 2020;12(2):022003. doi:10.1088/1758-5090/ab6f0d
22. Ogunsanya M, Desai S. Predictive modeling of additive manufacturing process using deep learning algorithm. In: Ellis K, Ferrell W, Knapp J, eds. Proceedings of the IISE Annual Conference & Expo 2022. Institute of Industrial and Systems Engineers; 2022. https://par.nsf.gov/servlets/purl/10347277
23. Isichei JC, Khorsandroo S, Desai S. Cybersecurity and privacy in smart bioprinting. Bioprinting. 2023;36:e00321. doi:10.1016/j.bprint.2023.e00321
24. Nandipati M, Fatoki O, Desai S. Bridging nanomanufacturing and artificial intelligence—a comprehensive review. Materials (Basel). 2024;17(7):1621. doi:10.3390/ma17071621
25. Ogunsanya M, Isichei J, Desai S. Grid search hyperparameter tuning in additive manufacturing processes. Manuf Lett. 2023;35:1031-1042. doi:10.1016/j.mfglet.2023.08.056
26. Ng WL, et al. Advanced bioprinting strategies for fabrication of biomimetic tissues and organs. Int. J. Extrem. Manuf. 2025; **7**:062006
27. Huang W, Chen S, Li K, et al. Nanoengineered extrusion-aligned tract bioprinting enables functional repair of spinal cord injuries. Cell Stem Cell. 2026;33(2):340-354.e7. doi:10.1016/j.stem.2025.12.021
28. Lee JS, Cha JH, Kim, BS. Artificial intelligence in 3D bioprinting and biofabrication: a validation-stringency assessment. Biofabrication. 2026;18(3):032003. doi:10.1088/1758-5090/ae7b07
29. Zhang C, Elvitigala KCML, Sakai S. Generative AI-guided in silico closed-loop optimisation of deposition morphology for 3D bioprinting applications. Virtual and Phys. Prototyp. 2026;21(1). doi: 10.1080/17452759.2026.2671497.
30. Yu C, Jiang J. A perspective on using machine learning in 3D bioprinting. Int J Bioprint. 2020;6(1):253. doi:10.18063/ijb.v6i1.253

31. Bonatti AF, Vozzi G, De Maria C. Enhancing quality control in bioprinting through machine learning. Biofabrication. 2024;16(2):022001. doi:10.1088/1758-5090/ad2189
32. Armstrong AA, Norato J, Alleyne AG, Wagoner Johnson AJ. Direct process feedback in extrusion-based 3D bioprinting. Biofabrication. 2020;12(1):015017. doi:10.1088/1758-5090/ab4d97
33. Krishna DV, Sankar MR. Machine learning-assisted extrusion-based 3D bioprinting for tissue regeneration applications. Ann 3D Print Med. 2023;12:100132. doi:10.1016/j.stlm.2023.100132
34. An J, Chua CK, Mironov V. Application of machine learning in 3D bioprinting: focus on development of big data and digital twin. Int J Bioprint. 2021;7(1):342. doi:10.18063/ijb.v7i1.342
35. Ramesh S, Deep A, Tamayol A, Kamaraj AB, Mahajan C, Madihally S. Advancing 3D bioprinting through machine learning and artificial intelligence. Bioprinting. 2024;38:e00331. doi:10.1016/j.bprint.2024.e00331
36. Wang J, Cui Z, Maniruzzaman M. Bioprinting: a focus on improving bioink printability and cell performance based on different process parameters. Int J Pharm. 2023;640:123020. doi:10.1016/j.ijpharm.2023.123020
37. Rahmani Dabbagh S, Ozcan O, Tasoglu S. Machine learning-enabled optimization of extrusion-based 3D printing. Methods. 2022;206:27-40. doi:10.1016/j.ymeth.2022.08.002
38. Fu Z, Angeline V, Sun W. Evaluation of printing parameters on 3D extrusion printing of Pluronic hydrogels and machine learning guided parameter recommendation. Int J Bioprint. 2021;7(4):434. doi:10.18063/ijb.v7i4.434
39. Ruberu K, Senadeera M, Rana S, et al. Coupling machine learning with 3D bioprinting to fast track optimisation of extrusion printing. Appl Mater Today. 2021;22:100914. doi:10.1016/j.apmt.2020.100914
40. Bonatti AF, Vozzi G, Chua CK, De Maria C. A deep learning quality control loop of the extrusion-based bioprinting process. Int J Bioprint. 2022;8(4):620. doi:10.18063/ijb.v8i4.620
41. Conev A, Litsa EE, Perez MR, Diba M, Mikos AG, Kavraki LE. Machine learning-guided three-dimensional printing of tissue engineering scaffolds. Tissue Eng Part A. 2020;26(23-24):1359-1368. doi:10.1089/ten.tea.2020.0191

42. Rafieyan S, Vasheghani-Farahani E, Baheiraei N, Keshavarz H. MLATE: machine learning for predicting cell behavior on cardiac tissue engineering scaffolds. Comput Biol Med. 2023;158:106804. doi:10.1016/j.compbiomed.2023.106804
43. Williams D, Thayer P, Martinez H, Gatenholm E, Khademhosseini A. A perspective on the physical, mechanical and biological specifications of bioinks and the development of functional tissues in 3D bioprinting. Bioprinting. 2018;9:19-36. doi:10.1016/j.bprint.2018.02.003
44. Sun J, Yao K, An J, Jing L, Huang K, Huang D. Machine learning and 3D bioprinting. Int J Bioprint. 2023;9(4):717. doi:10.18063/ijb.717
45. Suntornnond R, Tan EYS, An J, Chua CK. A highly printable and biocompatible hydrogel composite for direct printing of soft and perfusable vasculature-like structures. Sci Rep. 2017;7(1):16902. doi:10.1038/s41598-017-17198-0
46. Hu T, Cai Z, Yin R, Zhang W, Bao C, Zhu L, Zhang H. 3D Embedded Printing of Complex Biological Structures with Supporting Bath of Pluronic F-127. Polymers. 2023; 15(17):3493. doi:10.3390/polym15173493
47. Muñoz-Pérez E, Pérez-Valle A, Igartua M, Santos-Vizcaíno E, Hernández RM. High resolution and fidelity 3D printing of Laponite and alginate ink hydrogels for tunable biomedical applications. Biomater Adv. 2023;149:213414. doi:10.1016/j.bioadv.2023.213414
48. Axpe E, Oyen ML. Applications of Alginate-Based Bioinks in 3D Bioprinting. Int J Mol Sci. 2016; 17(12):1976. doi:10.3390/ijms17121976
49. Kolesky DB, Truby RL, Gladman AS, Busbee TA, Homan KA, Lewis JA. 3D bioprinting of vascularized, heterogeneous cell-laden tissue constructs. *Adv Mater*. 2014;26(19):3124-3130. doi:10.1002/adma.201305506
50. Gao Q, Kim B-S, Gao G. Advanced Strategies for 3D Bioprinting of Tissue and Organ Analogs Using Alginate Hydrogel Bioinks. Mar Drugs. 2021; 19(12):708. doi:10.3390/md19120708
51. Guvendiren M, Molde J, Soares RMD, Kohn J. Designing biomaterials for 3D printing. ACS Biomater Sci Eng. 2016;2(10):1679-1693. doi:10.1021/acsbiomaterials.6b00121

52. Gillispie GJ, Han A, Uzun-Per M, et al. The Influence of Printing Parameters and Cell Density on Bioink Printing Outcomes. Tissue Eng Part A. 2020;26(23-24):1349-1358. doi:10.1089/ten.TEA.2020.0210
53. Gillispie GJ, Copus J, Uzun-Per M, et al. The correlation between rheological properties and extrusion-based printability in bioink artifact quantification. Mater Des. 2023;233:112237. doi:10.1016/j.matdes.2023.112237
54. Kalantary S, Jahani A, Jahani R. MLR and ANN approaches for prediction of synthetic/natural nanofibers diameter in environmental and medical applications. Sci Rep. 2020;10(1):8117. doi:10.1038/s41598-020-65121-x
55. He H, Yang Y, Pan Y. Machine learning for continuous liquid interface production: printing speed modelling. J Manuf Syst. 2019;50:236-246. doi:10.1016/j.jmsy.2019.01.004
56. Zanderigo G, Bracco F, Semeraro Q, Colosimo BM. In-situ printability maps: a new approach for in-situ printability assessment with application to extrusion-based bioprinting. Bioprinting. 2023;36:e00320. doi:10.1016/j.bprint.2023.e00320
57. Jin Z, Zhang Z, Shao X, Gu GX. Monitoring anomalies in 3D bioprinting with deep neural networks. ACS Biomater Sci Eng. 2023;9(7):3945-3952. doi:10.1021/acsbiomaterials.0c01761
58. Hastie T, Tibshirani R, Friedman J. *The Elements of Statistical Learning: Data Mining, Inference, and Prediction*. 2nd ed. Springer; 2009. doi:10.1007/978-0-387-84858-7
59. Chen H, Liu Y, Balabani S, Hirayama R, Huang J. Machine learning in predicting printable biomaterial formulations for direct ink writing. Research (Wash D C). 2023;6:0197. doi:10.34133/research.0197
60. Malekpour A, Chen X. Printability and cell viability in extrusion-based bioprinting from experimental, computational, and machine learning views. J Funct Biomater. 2022;13(2):40. doi:10.3390/jfb13020040
61. Xu H, Liu Q, Casillas J, et al. Prediction of cell viability in dynamic optical projection stereolithography-based bioprinting using machine learning. J Intell Manuf. 2022;33(4):995-1005. doi:10.1007/s10845-020-01708-5